Deconvolution of SNPP VIIRS Solar Diffuser Bidirectional Reflectance Distribution Function On-orbit Change Factor

Ning Lei* and Xiaoxiong Xiong

Abstract—**The Earth-observing Visible Infrared Imaging Radiometer Suite (VIIRS) on the Suomi National Polar-orbiting Partnership satellite regularly calibrates its reflective solar bands (RSBs), primarily through observing an onboard sunlit solar diffuser (SD). The on-orbit change of the value of the SD bidirectional reflectance distribution function (BRDF) is quantified by a numerical factor, called the H-factor, and is determined by the onboard SD stability monitor (SDSM). Because the spectral response function of an SDSM detector spreads in wavelength, the directly measured H-factor is the true H-factor convolved with the spectral response function. To find the true H-factor, we use the traditional direct method and an innovative iterative approach to separately deconvolve the measured H-factor. Our iterative approach relies on two properties of the SDSM detector spectral response function: the central peak width is narrow enough so that the H-factor does not change much over the peak width, and the dominance of the spectral response function's integral with respect to the wavelength over the width. The iterative approach is more accurate, of a smaller noise impact, much more flexible in terms of interpolation and extrapolation of function values, and faster. We have used deconvolved H-factors to calibrate the NASA SNPP VIIRS RSB Collections 1 and 2 Level-1B products.**

Index Terms: SNPP VIIRS, radiometric calibration, reflective solar band, solar diffuser, BRDF change, H-factor, deconvolution

I. INTRODUCTION

The Visible Infrared Imaging Radiometer Suite (VIIRS) is an Earth-observing satellite sensor, collecting data to generate more than 20 biogeophysical parameters for Earth studies [1-3]. VIIRS continues the data collection missions of the Moderate Resolution Imaging Spectroradiometers (MODISs) on Terra and Aqua satellites [4], [5]. Among the 22 VIIRS spectral bands, 14 are the reflective solar bands (RSBs), designed to detect the Earth reflected sunlight, with band center wavelengths from 0.412 to 2.250 μm [6]. Each VIIRS band has an array of detectors. The VIIRS imaging and moderate resolution bands have spatial resolutions at nadir of 375 m and 750 m, respectively. Three of the 14 RSBs are the imaging bands and the rest are the moderate resolution bands. The first VIIRS instrument is aboard the Suomi National Polar-orbiting Partnership (SNPP) satellite launched on October 28, 2011. The SNPP satellite has a mean altitude of 839 km and is maintained in a near Sun-synchronous orbit with an equator-crossing local time of 13:30 [7], [8].

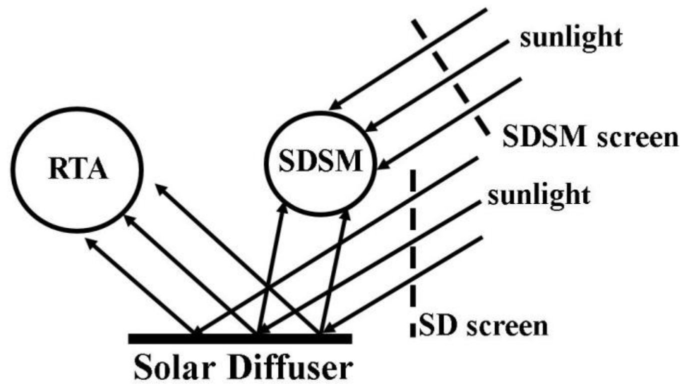

Fig. 1. A schematic representation of the physical components related to the on-orbit RSB radiometric calibration of VIIRS. The RTA is the rotating telescope assembly which directs incident light to the detector focal planes.

TABLE I
SDSM DETECTOR DESIGN CENTER WAVELENGTHS

Detector	Band centers (μm)
1	0.412
2	0.445
3	0.488
4	0.555
5	0.672
6	0.745
7	0.865
8	0.926

We calibrate the VIIRS RSBs through an onboard solar diffuser (SD) when the SD is fully solar illuminated through the SD screen [6], [9], as illustrated in Fig. 1. The SD diffusely scatters sunlight to provide a known spectral radiance for the calibration. The change in the SD bidirectional reflectance distribution function (BRDF) value since launch is commonly quantified by a numerical factor known as the H-factor [6], [10]. The H-factor is determined by an onboard SD stability monitor (SDSM) through a ratio approach. When in operation, the SDSM observes the Sun and the SD at almost the same time. The ratio of the SDSM detector signal strengths over the SD and the Sun views is a measure of the H-factor. The 8 SDSM

* Ning Lei is with the Science Systems and Applications, Inc., Lanham, MD 20706 USA (e-mail: ning.lei@ssaihq.com).

Xiaoxiong Xiong is with Sciences and Exploration Directorate, NASA Goddard Space Flight Center, Greenbelt, MD 20771 USA (e-mail: xiaoxiong.xiong-1@nasa.gov).

detectors cover wavelengths from 0.412 to 0.926 μm. Table I lists the design detector center wavelengths of the 8 SDSM detectors.

Because the SDSM detector spectral response function spreads in wavelength, the directly measured H-factor through the ratio approach, denoted by $H_{\mathrm{SDSM}}^{\mathrm{mea}}$, is the true H-factor, denoted by H_{SDSM}, convolved with the spectral response function [14]:

$$H_{\mathrm{SDSM}}^{\mathrm{mea}}\left(\lambda_d, t, \vec{\phi}(t)\right) = \frac{\int_0^\infty d\lambda \times \mathrm{SR}_{\mathrm{SDSM}}(\lambda,t,d)\Phi_{\mathrm{SUN}}(\lambda,t) H_{\mathrm{SDSM}}\left(\lambda,t,\vec{\phi}(t)\right)}{\int_0^\infty d\lambda \times \mathrm{SR}_{\mathrm{SDSM}}(\lambda,t,d)\Phi_{\mathrm{SUN}}(\lambda,t)}\ , \quad (1)$$

where $\mathrm{SR}_{\mathrm{SDSM}}$ denotes the SDSM detector spectral response function, λ_d is the detector center wavelength, *t* is time, $\vec{\phi}(t)$ is the solar angle at *t*, λ is the sunlight wavelength, *d* is the SDSM detector index, and Φ_{SUN} is the solar spectral power. $\mathrm{SR}_{\mathrm{SDSM}}(\lambda, t = 0, d)$ is derived from the prelaunch measurements of the SDSM fold mirror reflectivity, the reflectance of the SDSM Spherical Integrating Source, the transmittance of the SDSM detector bandpass filter, and the SDSM detector quantum efficiency. The values from these measurements are proprietary and hence are not given in this paper. The bandpass filter transmittance depends on filter orientation. Because we do not know the orientation, we use the transmittance averaged over the orientations. $\Phi_{\mathrm{SUN}}(\lambda,\ t = 0)$ is from MODTRAN Version 4.3 Revision 1 (SNPP VIIRS Sensor Data Record meeting archive). The change of $\mathrm{SR}_{\mathrm{SDSM}}(\lambda,t,d)\Phi_{\mathrm{SUN}}(\lambda,t)$ since the satellite launch is determined by using the normalized SDSM detector Sun view digital count [14], as shown in APPENDIX A, through solving another integral equation.

To obtain the true H-factor, we need to deconvolve the measured H-factor. In this paper, we first use the popular direct method [11-13] to deconvolve the measured H-factor (Section II). We then use an innovative approach to iteratively deconvolve the measured H-factor. In the iterative approach, we use the properties that the SDSM detector spectral response function's central peak width is narrow enough so that the H-factor does not change excessively over the peak width and the dominance of the spectral response function's integral with respect to the wavelength over the width (Section III). We compare the two approaches in terms of accuracy, computation speed, and robustness against the noise in the measured H-factor (Section IV). We also give examples of our iterative deconvolution approach with Gaussian detector response functions (Section V) and show the impacts of the deconvolved H-factor on the retrieved SNPP VIIRS Earth scene solar spectral reflectance (Section VI).

II. DIRECT METHOD TO DECONVOLVE MEASURED H-FACTOR

To simplify the notation in (1), we define the modified spectral response function:

$$\mathrm{SR}'_{\mathrm{SDSM}}(\lambda,t,d) = \frac{\mathrm{SR}_{\mathrm{SDSM}}(\lambda,t,d)\Phi_{\mathrm{SUN}}(\lambda,t)}{\int_0^\infty d\lambda \times \mathrm{SR}_{\mathrm{SDSM}}(\lambda,t,d)\Phi_{\mathrm{SUN}}(\lambda,t)}\ , \quad (2)$$

and re-write (1) as

$$H_{\mathrm{SDSM}}^{\mathrm{MEA}}\left(\lambda_d, t, \vec{\phi}(t)\right) = \int_0^\infty d\lambda \times \mathrm{SR}'_{\mathrm{SDSM}}(\lambda,t,d) \times H_{\mathrm{SDSM}}\left(\lambda, t, \vec{\phi}(t)\right)\ . \quad (3)$$

In reality, the tabulated $\mathrm{SR}'_{\mathrm{SDSM}}(\lambda,t,d)$ has wavelength limits. We denote the minimum and maximum wavelengths by $\lambda_{\min}$ and $\lambda_{\max}$, respectively, and write (3) as

$$H_{\mathrm{SDSM}}^{\mathrm{mea}}\left(\lambda_d, t, \vec{\phi}(t)\right) = \int_{\lambda_{\min}}^{\lambda_{\max}} d\lambda \times \mathrm{SR}'_{\mathrm{SDSM}}(\lambda,t,d) \times H_{\mathrm{SDSM}}\left(\lambda, t, \vec{\phi}(t)\right). \quad (4)$$

For the tabulated SNPP VIIRS $\mathrm{SR}'_{\mathrm{SDSM}}(\lambda,t,d)$, the wavelength limits are 0.3 μm and 1.2 μm, respectively. In this section, we directly solve (4) to find H_{SDSM}.

We denote the 8 SDSM detector center wavelengths by λ_1, λ_2,…, λ_8, the H_{SDSM} at the 8 center wavelengths by H_1, H_2, …, H_8, and the $H_{\mathrm{SDSM}}^{\mathrm{mea}}$ at the 8 center wavelengths by $H_1^{\mathrm{mea}}, H_2^{\mathrm{mea}}, \ldots, H_8^{\mathrm{mea}}$. We define the detector center wavelength as the center of the response function's main peak in the sense that the area under the response function vs wavelength curve from the lower end of the main peak to the center is the same as that from the center to the higher end. At the lower and higher ends of main peak wavelengths, the response function values are at 1% of the maximum peak value. We use $H_{\max}$ to denote the H_{SDSM} at $\lambda_{\max}$. We have observed that the H-factor generally decreases over time from the original value of 1 and is larger at a longer wavelength after the mission start [10], [15]. At the SDSM detector 8 center wavelength of a nominal value of 0.926 μm, the H-factor is close to 1. Hence, at $\lambda_{\max}$ of 1.199 μm, it is reasonable to set $H_{\max}$=1. At a wavelength between two detector center wavelengths or between λ_8 and $\lambda_{\max}$, we linearly interpolate the corresponding H_{SDSM}. At a wavelength less than λ_1, we linearly extrapolate H_1 and H_2.

An event that occurred on February 24, 2019 impacted the SD screen and/or the SD, resulting in sudden drops in the measured H-factors across the event time. For the H-factor directly measured by the SDSM detector 8, the drop is 0.7%. Hence, after February 24, 2019, we set $H_{\max} = 0.993$.

From (4), we have the following equation:

$$\begin{aligned} H_d^{\mathrm{mea}} = &\int_{\lambda_{\min}}^{\lambda_2} d\lambda \times \mathrm{SR}'_{\mathrm{SDSM}}(\lambda,t,d) \times \left(a_{1,1} + a_{1,2}\lambda\right) + \\ &\int_{\lambda_2}^{\lambda_3} d\lambda \times \mathrm{SR}'_{\mathrm{SDSM}}(\lambda,t,d) \times \left(a_{2,1} + a_{2,2}\lambda\right) + \cdots + \\ &\int_{\lambda_7}^{\lambda_8} d\lambda \times \mathrm{SR}'_{\mathrm{SDSM}}(\lambda,t,d) \times \left(a_{7,1} + a_{7,2}\lambda\right) + \\ &\int_{\lambda_8}^{\lambda_{\max}} d\lambda \times \mathrm{SR}'_{\mathrm{SDSM}}(\lambda,t,d) \times \left(a_{8,1} + a_{8,2}\lambda\right)\ , \end{aligned} \quad (5)$$

where *d*=1, 2, …, 8, and the coefficients $a_{1,1}$, $a_{1,2}$, ⋯, $a_{8,2}$ are obtained through the constraint that at a detector center wavelength, the corresponding linear polynomial, such as

$a_{1,1} + a_{1,2}\lambda$, yields a value that equals to the true H-factor at the wavelength. For example,

$$a_{1,1} = \frac{\lambda_2 H_1 - \lambda_1 H_2}{\lambda_2 - \lambda_1}, \tag{6}$$

and

$$a_{1,2} = \frac{H_2 - H_1}{\lambda_2 - \lambda_1} \quad . \tag{7}$$

Inserting (6), (7), and the similar mathematical expressions for the other coefficients into (5), we have

$$H_d^{\text{mea}} = H_1 \int_{\lambda_{\min}}^{\lambda_2} d\lambda \times \text{SR}'_{\text{SDSM}}(\lambda, t, d) \times \frac{\lambda_2 - \lambda}{\lambda_2 - \lambda_1} + H_2 \left[\int_{\lambda_{\min}}^{\lambda_2} d\lambda \times \text{SR}'_{\text{SDSM}}(\lambda, t, d) \times \frac{\lambda - \lambda_1}{\lambda_2 - \lambda_1} + \int_{\lambda_2}^{\lambda_3} d\lambda \times \text{SR}'_{\text{SDSM}}(\lambda, t, d) \times \frac{\lambda_3 - \lambda}{\lambda_3 - \lambda_2}\right] + \cdots + H_8 \left[\int_{\lambda_7}^{\lambda_8} d\lambda \times \text{SR}'_{\text{SDSM}}(\lambda, t, d) \times \frac{\lambda - \lambda_7}{\lambda_8 - \lambda_7} + \int_{\lambda_8}^{\lambda_{\max}} d\lambda \times \text{SR}'_{\text{SDSM}}(\lambda, t, d) \times \frac{\lambda_{\max} - \lambda}{\lambda_{\max} - \lambda_8}\right] + H_{\max} \int_{\lambda_8}^{\lambda_{\max}} d\lambda \times \text{SR}'_{\text{SDSM}}(\lambda, t, d) \times \frac{\lambda - \lambda_8}{\lambda_{\max} - \lambda_8}. \tag{8}$$

We write (8) into a matrix form of

$$\begin{pmatrix} H_1^{\text{MEA}} - c_1 \\ H_2^{\text{MEA}} - c_2 \\ \vdots \\ H_8^{\text{MEA}} - c_8 \end{pmatrix} = \begin{pmatrix} b_{1,1} & b_{1,2} & \cdots & b_{1,8} \\ & & \vdots & \\ b_{8,1} & b_{8,2} & \cdots & b_{8,8} \end{pmatrix} \begin{pmatrix} H_1 \\ H_2 \\ \vdots \\ H_8 \end{pmatrix}, \tag{9}$$

where

$$c_d = H_{\max} \int_{\lambda_8}^{\lambda_{\max}} d\lambda \times \text{SR}'_{\text{SDSM}}(\lambda, t, d) \times \frac{\lambda - \lambda_8}{\lambda_{\max} - \lambda_8}, \tag{10}$$

$$b_{d,1} = \int_{\lambda_{\min}}^{\lambda_2} d\lambda \times \text{SR}'_{\text{SDSM}}(\lambda, t, d) \times \frac{\lambda_2 - \lambda}{\lambda_2 - \lambda_1}, \tag{11}$$

$$b_{d,2} = \left[\int_{\lambda_{\min}}^{\lambda_2} d\lambda \times \text{SR}'_{\text{SDSM}}(\lambda, t, d) \times \frac{\lambda - \lambda_1}{\lambda_2 - \lambda_1} + \int_{\lambda_2}^{\lambda_3} d\lambda \times \text{SR}'_{\text{SDSM}}(\lambda, t, d) \times \frac{\lambda_3 - \lambda}{\lambda_3 - \lambda_2}\right], \tag{12}$$

$$b_{d,3} = \left[\int_{\lambda_2}^{\lambda_3} d\lambda \times \text{SR}'_{\text{SDSM}}(\lambda, t, d) \times \frac{\lambda - \lambda_2}{\lambda_3 - \lambda_2} + \int_{\lambda_3}^{\lambda_4} d\lambda \times \text{SR}'_{\text{SDSM}}(\lambda, t, d) \times \frac{\lambda_4 - \lambda}{\lambda_4 - \lambda_3}\right], \tag{13}$$

etc, and

$$b_{d,8} = \int_{\lambda_7}^{\lambda_8} d\lambda \times \text{SR}'_{\text{SDSM}}(\lambda, t, d) \times \frac{\lambda - \lambda_7}{\lambda_8 - \lambda_7} + \int_{\lambda_8}^{\lambda_{\max}} d\lambda \times \text{SR}'_{\text{SDSM}}(\lambda, t, d) \times \frac{\lambda_{\max} - \lambda}{\lambda_{\max} - \lambda_8}. \tag{14}$$

The summation of $b_{d,1}, b_{d,2}, \cdots, b_{d,8}$ is

$$b_{d,1} + b_{d,2} + \cdots + b_{d,8} = \int_{\lambda_{\min}}^{\lambda_8} d\lambda \times \text{SR}'_{\text{SDSM}}(\lambda, t, d) + \int_{\lambda_8}^{\lambda_{\max}} d\lambda \times \text{SR}'_{\text{SDSM}}(\lambda, t, d) \times \frac{\lambda_{\max} - \lambda}{\lambda_{\max} - \lambda_8}. \tag{15}$$

For $d \neq 8$, the integral of SR'_{SDSM} over the wavelength region of λ_8 to $\lambda_{\max}$ is extremely small. Hence the summation is approximately 1. For d=8, the summation is slightly less than 1 because over the region of λ_8 to $\lambda_{\max}$, $\lambda_{\max} - \lambda$ is less than or equal to $\lambda_{\max} - \lambda_8$. We call the matrix formed by $b_{d,i}$, with d=1-8 and i=1-8, the B-matrix. All elements in the B-matrix are non-negative. The diagonal elements of the B-matrix are relatively large, close to but less than 1 because each of the elements contains the in-band integral of SR'_{SDSM}.

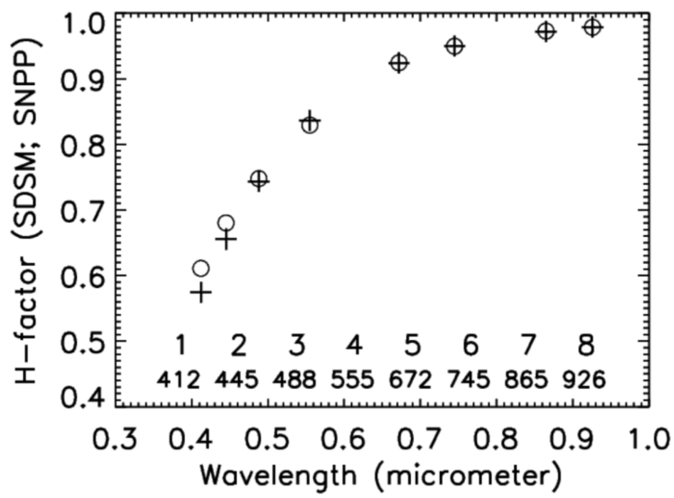

Fig. 2. Measured (circles) and deconvolved (pluses) SNPP VIIRS SD H-factors for the SDSM SD view at day 2621 after the satellite launch, with the direct method. The SDSM detector indexes are shown in the figure. Right below each detector index is the design detector center wavelength in nanometers.

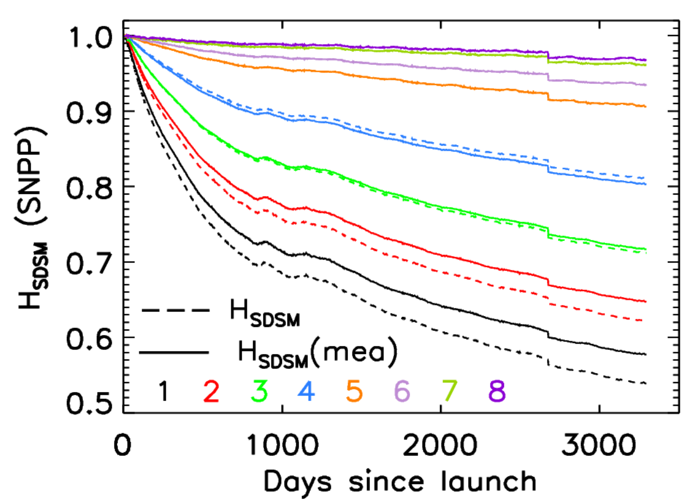

Fig. 3. Measured (solid lines) and deconvolved (dashed lines) SNPP VIIRS SD H-factors at the SDSM SD view, versus time since the satellite launch, with the direct method. The SDSM detector indexes are shown in the figure.

Solving (9), we find H_1, H_2, …, and H_8 from $H_1^{\text{mea}}, H_2^{\text{mea}}, \ldots$, and H_8^{mea}. As an example, in Fig. 2 we show the measured and the deconvolved H-factors versus the SDSM detector center wavelengths at day 2621 since the satellite launch. Fig. 2 shows that the measured H-factors vary monotonically with the wavelength. The difference between the measured and the deconvolved H-factors decreases rapidly toward longer wavelengths. The deconvolved H-factors differ from the corresponding measured H-factors by zero amount at the mission start and the differences increase with time, as shown in Fig. 3. At the SDSM detector 1 center wavelength and the most recent time in the figure, the difference is -6.6%. On the other hand, at the SDSM detector 5-8 center wavelengths, the difference magnitudes are less than 0.1% at all times, a result of the flattening of the H-factor versus wavelength curve toward longer wavelengths.

III. ITERATIVE APPROACH TO DECONVOLVE MEASURED H-FACTOR

To solve the integral equation (4), we consider that the SDSM detector spectral response function strongly peaks approximately at the detector center wavelength with a narrow in-band width of tens of nanometers within which the H-factor does not vary much. Hence we can approximate (4) by [16]

$$H_{\mathrm{SDSM}}^{\mathrm{mea}}\left(\lambda_d, t, \vec{\phi}(t)\right) = H_{\mathrm{SDSM}}\left(\lambda_d, t, \vec{\phi}(t)\right) \int_{\mathrm{in-band}} d\lambda \times \mathrm{SR}'_{\mathrm{SDSM}}(\lambda, t, d) + \int_{\mathrm{OOB}} d\lambda \times \mathrm{SR}'_{\mathrm{SDSM}}(\lambda, t, d) \times H_{\mathrm{SDSM}}\left(\lambda, t, \vec{\phi}(t)\right), \quad (16)$$

where OOB indicates the out-of-band wavelength region. In this study, the in-band wavelength cutoffs are at 1% of the main peak value of the spectral response function—the exact percentage as the criterion for the cutoffs does not have meaningful impacts on the deconvolved H-factor. Because the in-band contribution of the $\mathrm{SR}'_{\mathrm{SDSM}}$ integral dominates, in the first iteration, we ignore the out-of-band contribution in (16) to yield

$$H_{\mathrm{SDSM}}\left(\lambda_d, t, \vec{\phi}(t); 1\mathrm{st}\right) = \frac{H_{\mathrm{SDSM}}^{\mathrm{mea}}\left(\lambda_d, t, \vec{\phi}(t)\right)}{\int_{\mathrm{in-band}} d\lambda \times \mathrm{SR}'_{\mathrm{SDSM}}(\lambda, t, d)}, \quad (17)$$

where the “1st” means the first iteration.

In the second iteration, we account for the out-of-band contribution in (16) to arrive at

$$H_{\mathrm{SDSM}}^{\mathrm{mea}}\left(\lambda_d, t, \vec{\phi}(t)\right) = H_{\mathrm{SDSM}}\left(\lambda_d, t, \vec{\phi}(t); 2\mathrm{nd}\right) \int_{\mathrm{in-band}} d\lambda \times \mathrm{SR}'_{\mathrm{SDSM}}(\lambda, t, d) + \int_{\mathrm{OOB}} d\lambda \times \mathrm{SR}'_{\mathrm{SDSM}}(\lambda, t, d) \times H_{\mathrm{SDSM}}\left(\lambda, t, \vec{\phi}(t); 1\mathrm{st}\right). \quad (18)$$

To calculate $H_{\mathrm{SDSM}}\left(\lambda, t, \vec{\phi}(t); 1\mathrm{st}\right)$, we linearly interpolate or extrapolate $H_{\mathrm{SDSM}}\left(\lambda_d, t, \vec{\phi}(t); 1\mathrm{st}\right)$ obtained in the first iteration with d=1, ⋯, 8 over the wavelengths up to 0.965 μm which is the upper limit of the detector 8 in-band wavelengths. Beyond 0.965 μm, $H_{\mathrm{SDSM}}\left(\lambda, t, \vec{\phi}(t); 1\mathrm{st}\right)$ is found by using a wavelength power law of

$$H_{\mathrm{SDSM}}\left(\lambda, t, \vec{\phi}(t); 1\mathrm{st}\right) = 1 - \frac{\left[1 - H_{\mathrm{SDSM}}\left(\lambda_8, t, \vec{\phi}(t); 1\mathrm{st}\right)\right] {\lambda_8}^{\eta_{\mathrm{H}}}}{\lambda^{\eta_{\mathrm{H}}}}, \quad (19)$$

where η_{H} is 4.07 from the mission start to February 24, 2019 and 3.67 after February 24, 2019. For the nth iteration (n>1), we have

$$H_{\mathrm{SDSM}}\left(\lambda_d, t, \vec{\phi}(t); n\mathrm{th}\right) = \frac{H_{\mathrm{SDSM}}^{\mathrm{mea}}\left(\lambda_d, t, \vec{\phi}(t)\right) - \int_{\mathrm{OOB}} d\lambda \times \mathrm{SR}'_{\mathrm{SDSM}}(\lambda, t, d) \times H_{\mathrm{SDSM}}\left(\lambda, t, \vec{\phi}(t); (n-1)\mathrm{th}\right)}{\int_{\mathrm{in-band}} d\lambda \times \mathrm{SR}'_{\mathrm{SDSM}}(\lambda, t, d)}. \quad (20)$$

We continue to iterate the procedure until the difference between the deconvolved H-factors in successive iterations is less than 0.0001. The number of iterations to reach the criterion is typically only 2 to 3.

After we obtain the stable H_{SDSM} from (20), we need to remove the impact of the H-factor curvature in wavelength. Even over the narrow range of the in-band wavelengths of tens of nanometers, the curvature can impact the H-factor by up to approximately 1.5% at the SDSM detector 1 center wavelength. The following example illustrates this point. Because the H-factor is roughly described by $1 - \frac{\beta_{\mathrm{H}}}{(\lambda/1\ \mu\mathrm{m})^4}$ [17], the H-factor versus wavelength curve has a negative curvature. Hence, averaging the H-factor over the in-band wavelengths yields a value that is smaller than the true H-factor. To reduce the curvature impact, we add the following to the H-factor obtained in (20):

$$\mathrm{deltaH} = \left(1 - \frac{\beta_{\mathrm{H}}}{(\lambda_d/1\mu\mathrm{m})^{\eta_{\mathrm{H}}}}\right) - \frac{\int_{\mathrm{in-band}} d\lambda \times \left(1 - \frac{\beta_{\mathrm{H}}}{(\lambda_d/1\mu\mathrm{m})^{\eta_{\mathrm{H}}}}\right) \times \mathrm{SR}'_{\mathrm{SDSM}}(\lambda, t, d)}{\int_{\mathrm{in-band}} d\lambda \times \mathrm{SR}'_{\mathrm{SDSM}}(\lambda, t, d)}, \quad (21)$$

where β_{H} and η_{H} are obtained from fitting the H-factor wavelength power law (see(23)) to the H_{SDSM} determined from (20) over two different wavelength segments, depending on the SDSM detector index. For a detector index of 1-4, the fit is over the H-factors for the SDSM detectors 1-4; a similar fit is for detectors 5-8. We fit the H-factors over the two segments because the wavelength power law with a single set of parameter values of β_{H} and η_{H} may not be statistically valid for the H-factors for all the SDSM detectors.

As expected, at a particular time and wavelength, the deconvolved H-factor from (20) is similar in value to that from the direct method, as shown in Fig. 4. As with Fig. 3, Fig. 4 shows that the deconvolved H-factor differs from the measured H-factor by a larger amount at a shorter wavelength when away from the mission start time. Additionally, at the respective center wavelengths of the SDSM detectors 5-8, the difference between the measured and the deconvolved H-factors is too small to be seen in Fig. 4.

Our iterative approach differs from the popular Van Cittert’s iterative deconvolution method [12], [18] in which in the first iteration, the true value is approximated by the measured value. In the second iteration, the measured value is predicted by performing the integral—in the H-factor case, it is the $\mathrm{SR}'_{\mathrm{SDSM}}$ integral with respect to the wavelength—by using the true value found in the first iteration. In this iteration, the true value is the summation of the one found in the first iteration and the difference between the actual measured and predicted measured values. For the subsequent iterations, the true value is the combination of the one found in the previous iteration and the difference between the measured value and the predicted measured value by using the true value found in the previous iteration.

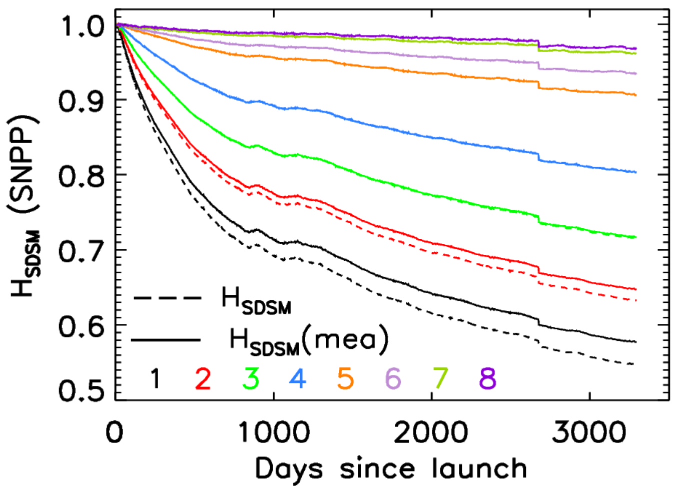

Fig. 4. Measured (solid lines) and deconvolved (dashed lines) SNPP VIIRS SD H-factors at the SDSM SD view, versus time since the satellite launch, with the iterative approach. The SDSM detector indexes are shown in the figure.

IV. COMPARE THE TWO APPROACHES

The deconvolved H-factors from the direct method and the iterative approach are not exactly the same, as shown in Figs. 3 and 4. At the SDSM detector 1 band center wavelength and the most recent time, the deconvolved H-factors from the direct method and the iterative approach are 0.539 and 0.547, respectively. Hence, we need to evaluate which approach yields more accurate results and which approach is less impacted by the noise in the measured H-factor. Finally, this section compares the deconvolution speeds of the two approaches.

The integral equation (3) is a Fredholm integral equation of the first kind [11]. Previous studies in the literature show that noise in the measured data may significantly affect the deconvolved value [11], [12]. In the direct method, the diagonal elements in the B-matrix are positive and less than 1, causing larger inaccuracy (than noise) in the deconvolved H-factor in the presence of noises in the measured H-factors. To see this point mathematically, we assume that SR'_{SDSM} is sharp enough so that, except the diagonal elements in the B-matrix in (9), the only non-zero B-matrix elements are the ones right next to the diagonal element in each row. Under this assumption, from (9) we obtain

$$H_1 = \frac{H_1^{\mathrm{mea}} - c_1 - \frac{b_{1,2} H_2^{\mathrm{mea}}}{b_{2,2}} + \frac{b_{1,2} b_{2,3} H_3}{b_{2,2}}}{b_{1,1} - \frac{b_{1,2} b_{2,1}}{b_{2,2}}}. \tag{22}$$

Equation (22) reveals that a slight noise in H_1^{mea} results in a larger shift in H_1 because the denominator is less than 1 and positive. In the iterative approach, the deconvolved H-factor at the *n*th iteration is calculated by (20). Because the denominator in (20) is close to but less than 1 and positive, the noise is also amplified in the deconvolved H-factor.

To quantitatively show how noise impacts the values of the deconvolved H-factors for both approaches, we add a 0.25% amount of noise to the measured H-factor for a single SDSM detector and no noise for the other SDSM detectors. For the SDSM detector 2, a 0.25% noise impacts the deconvolved H-factor from the direct method by no less than 0.35% at all times, as shown in Fig. 5(a). For the same detector, the same amount of noise impacts much less on the deconvolved H-factor for the iterative approach, by approximately 0.27%, as shown in Fig. 5(b). The noise added to the measured H-factor for a particular detector impacts minimally on the deconvolved H-factors for the other detectors, as shown in Fig. 5, for both approaches. The impacts from a 0.25% noise added to the measured H-factor of a single detector averaged over all mission orbits on which the SDSM operated properly are listed in Table II. It is clear from the table that the noise's impact on the deconvolved H-factor is larger for the direct method than the iterative approach for all detectors. Hence from the noise impact aspect, the iterative approach performs better.

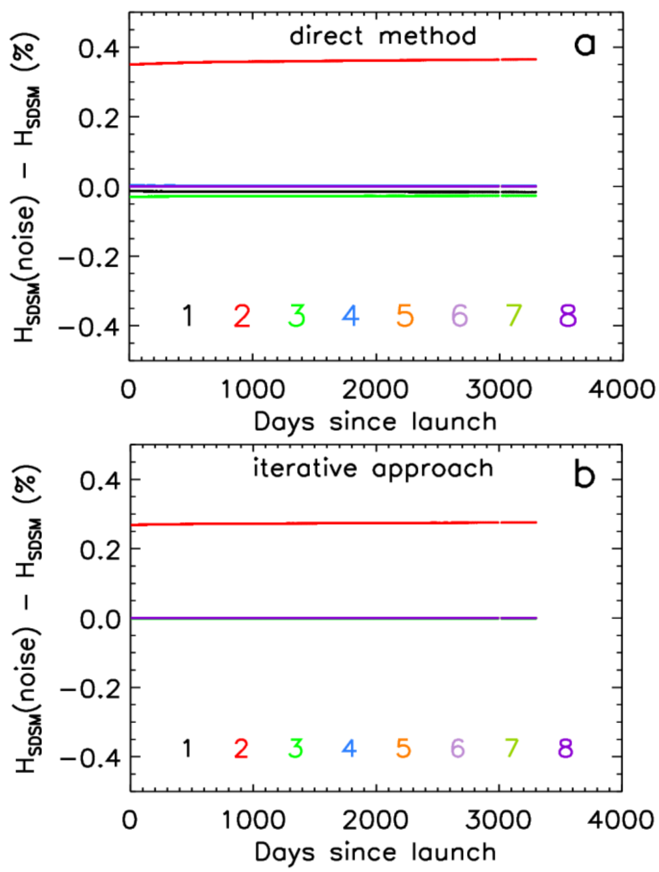

Fig. 5. Impact on the deconvolved H-factors after a 0.25% noise is added to the measured H-factor for the SDSM detector 2, for (a) the direct method, and (b) the iterative approach.

To address the accuracy of the deconvolved H-factor, we consider a set of hypothetical true H-factors and then find the corresponding measured H-factors by performing an SR' weighted H-factor integral with respect to the wavelength. We base the hypothetical true H-factors on a power law of the wavelength [15], [17], [19] in the form of

$$H(\lambda) = 1 - \frac{\beta_{\mathrm{H}}}{(\lambda/1\ \mu\mathrm{m})^{\eta_{\mathrm{H}}}}. \tag{23}$$

We set $\eta_{\mathrm{H}} = 4$ and $\beta_{\mathrm{H}} = 0.0133$. The iterative approach yields deconvolved H-factors that are very close to those calculated from (23), with the largest difference magnitude of 0.05%, occurring for detector 1. For the direct method, the largest difference has a much larger magnitude of 0.67%, occurring for detector 2. For all the SDSM detectors, the iterative approach deconvolves more accurately than the direct method. The differences in percentage for all detectors for both approaches are listed in Table III. The better accuracy from the iterative approach results from accounting for the H-factor curvature impact as we did in (21). Without accounting for the curvature impact, the direct method yields more accurate results. For example, at the SDSM detector 1 center wavelength, without the curvature correction, the iterative approach yields an H-factor which is 1.29% less than the hypothetical true H-factor.

TABLE II
CHANGE IN PERCENTAGE OF THE DECONVOLVED H-FACTORS FROM A 0.25% NOISE ADDED TO THE MEASURED H-FACTOR OF A SINGLE DETECTOR

Detector	Iterative approach	Direct method
1	0.288	0.300
2	0.271	0.355
3	0.258	0.311
4	0.255	0.286
5	0.255	0.283
6	0.254	0.273
7	0.252	0.318
8	0.253	0.281

TABLE III
100*[H(DECONVOLVED) – H(TRUE)]/H(TRUE)

Detector	Iterative approach	Direct method
1	-0.05	-0.59
2	0.03	0.67
3	0.02	0.34
4	0.01	0.27
5	0.01	0.14
6	0.00	0.04
7	0.00	0.04
8	0.00	0.01

In addition to the accuracy and the noise impact differences between the two approaches, the direct method is also much less flexible. A simple quadratic interpolation makes the direct method much more complex and a wavelength power law extrapolation makes the direct method impossible.

The computation time spent on deconvolving the H-factor is mainly on calculating the SR' weighted integral with respect to the wavelength. Both approaches perform the integral from $\lambda_{\min}$ to $\lambda_{\max}$ for each SDSM detector. The actual computation time depends on the code structure and the computer hardware that performs the calculation. The iterative approach deconvolves the H-factor very quickly, using only approximately 10 s to deconvolve 2761 sets of measured H-factors—each set is for one satellite orbit—on a Dell Precision 7820 Tower workstation, using Interactive Data Language (IDL) code. The direct method deconvolves the H-factors at a much slower rate, using approximately 1000 s to deconvolve 2761 sets of measured H-factors on the same workstation.

V. Examples

In this section, we give two examples of applying our iterative approach to deconvolve the underlying function. In the examples, we use a Gaussian function to represent the modified spectral response function in (3). The underlying functions are $1 - 0.0133/\lambda^4$ and $1/\lambda^2$.

Example 1

In this example, we assume the true H-factor follows $1 - 0.0133/\lambda^4$ where λ is in micrometer. The measured H-factors from the 8 SDSM detectors are the true H-factor convolved with the respective modified detector spectral response functions without noise. We assume that the response functions for all the SDSM detectors are Gaussian functions with the same Gaussian width of 0.03 μm. We further assume that the band centers of the SDSM detectors are the same as the design values, shown in Table I.

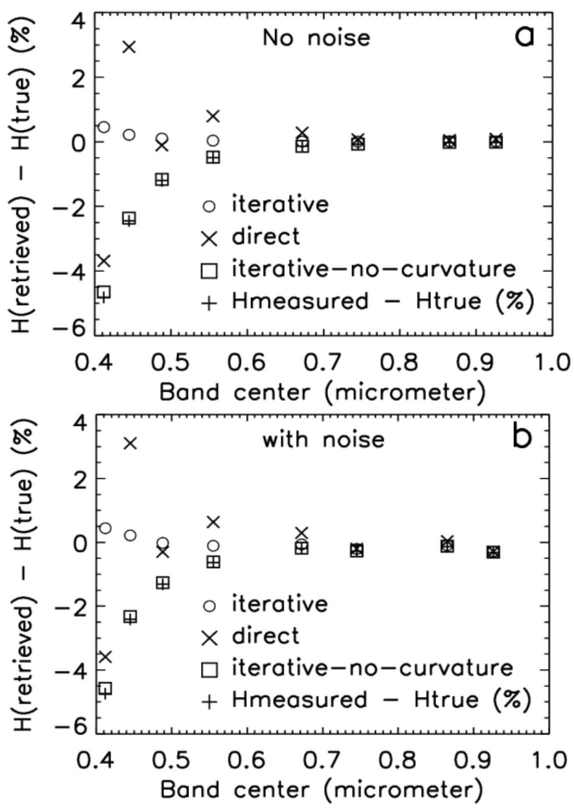

Fig. 6. Difference between the retrieved and the hypothetical true H-factors in percentage of the hypothetical true H-factor, using our iterative approach and the direct method. The circles and the squares are for the iterative approach with and without the curvature correction, respectively. The pluses are for the difference between the measured H-factor and the hypothetical true H-factor. (a) No noise; (b) with a Gaussian noise of the Gaussian width of 0.25%. With the noise, the measured H-factor becomes (1+noise)*(measured H-factor). The hypothetical true H-factor follows $1-0.0133/\lambda^4$ where λ is in micrometer. The detector spectral response function is a Gaussian function with the Gaussian width of 0.03 μm.

We use both the direct method and the iterative approach, as shown in Sections II and III, respectively, to deconvolve the H-factors. We first deconvolve the H-factors without any noise in the measured H-factors. As we mentioned in Section III, the curvature correction is very important in the iterative approach. Without the curvature correction, the deconvolved H-factors from the iterative approach can give inferior results compared with the ones from the direct method. With the curvature correction, the iterative approach yields results that are much closer to the hypothetical true H-factors than the ones from the direct method, as shown in Fig. 6(a). Separately, we add Gaussian noises, with the noise Gaussian width of 0.25% to the measured H-factors. The deconvolved H-factors do not differ much from ones for the no-noise case, as shown in Fig. 6(b). Note that in Fig. 4, for the SDSM detectors 1-3, the retrieved H-factors are smaller than the respective measured H-factors. This is because the solar spectrum peak wavelength is longer than the center wavelengths of these detectors, resulting in that SR' has a larger right tail than the left tail, coupled with the fact that the H-factor increases toward a longer wavelength. On the other hand, in this example, the true and retrieved H-factors are larger than the measured H-factors for these detectors (For detector 1, the measured H-factor is smaller than the true H-factor by 4.8%.), a result of a spectral response function that is symmetric around its central peak and an H-factor that decreases faster toward a shorter wavelength.

Finally, the large errors for the H-factors deconvolved by using the direct method likely come from the error brought by the linear interpolation. The iterative approach tolerates such interpolation error much better.

Example 2

In this example, we assume the underlying function is $1/\lambda^2$. The measurements are at 0.3 to 1.0 μm, with a step size of 0.1 μm, without noise. We assume that the response functions of the 8 band detectors are Gaussian functions with the same Gaussian width of 0.03 μm.

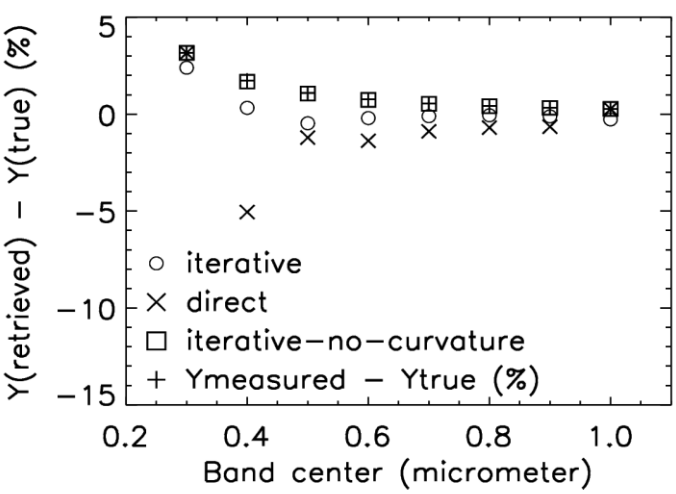

Fig. 7. Difference between the retrieved and the hypothetical true values in percentage of the hypothetical true values, using our iterative approach and the direct method. The circles and squares are for the iterative approach with and without curvature correction, respectively. The pluses are for the differences between the measured and the hypothetical true values. The hypothetical true value follows $1/\lambda^2$ where λ is in micrometer. The detector spectral response function is a Gaussian function with the Gaussian width of 0.03 μm.

Our iterative approach with the curvature correction gives the best results, as shown in Fig. 7. The largest error of approximately 2.4% occurs at 0.3 μm. At the band centers of the other 7 detectors, the error magnitudes are less than 0.5%. The direct approach yields a larger error of a magnitude of 5.1% at 0.4 μm, because of the linear interpolation approximation. Except at the detector 8 band center wavelength where the two approaches yield results which are of similar accuracy, at the rest detector center wavelengths, the iterative approach's results are of much higher accuracy.

Note in this example for the direct method, in (9) c_d (d=1, 2, …, 8) are zero. Additionally,

$$b_{d,8} = \int_{\lambda_7}^{\lambda_{\mathrm{MAX}}} d\lambda \times \mathrm{RSR}'_{\mathrm{SDSM}}(\lambda, t, d) \times \frac{\lambda-\lambda_7}{\lambda_8-\lambda_7} . \quad (24)$$

VI. IMPACTS OF DECONVOLVED H-FACTOR ON RETRIEVED VIIRS SCENE SPECTRAL REFLECTANCE

The impact of a deconvolved H-factor on the retrieved Earth view solar spectral reflectance is twofold. First, the deconvolved H-factor impacts the F-factor which is a retrieved scene spectral radiance correction factor. Currently, the F-factor calculated by using the sunlit SD needs to match the F-factor obtained through lunar observations—the lunar F-factor—up to a scale factor. Second, for the early missions of the subsequent VIIRS instruments, such as the NOAA-20 (N20) VIIRS, with the deconvolved H-factor for the SDSM SD view, we can apply the H_{SDSM}-to-H_{RTA} model parameter values obtained for the SNPP VIIRS to these instruments, such as the case for the N20 VIIRS [20]. In this section, we show the first impact.

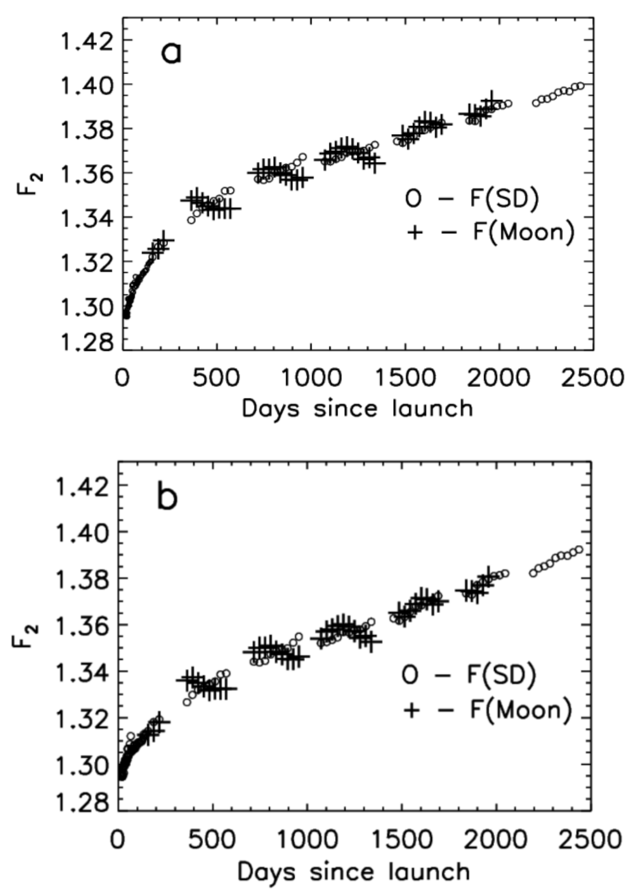

Fig. 8. The F-factors from the lunar observations (pluses) vs. the F-factors calculated by using (25) (circles). The parameter α_{RTA} is obtained by fitting the F_2 from (25) to the lunar F-factors from April 2012 to March 2017. The lunar F-factors has a multiplicative fitting parameter to account for the uncertainty in their absolute values. (a) Use H_{SDSM} in (25) as the independent parameter and (b) use $H_{\mathrm{SDSM}}^{\mathrm{mea}}$ to replace H_{SDSM} in (25).

We fit

$$F_2 = F_1(H_{\mathrm{SDSM}}) \times [1 + \alpha_{\mathrm{RTA}}(1 - H_{\mathrm{SDSM}})] \tag{25}$$

to the scaled lunar F-factors with the scale factor as a fitting parameter. The lunar F-factors are derived from the lunar observations made from April 2012 to March 2017 [21], [22]. In (25), $F_1(H_{\mathrm{SDSM}})$ denotes the F-factor calculated by using H_{SDSM} as the H-factor and divided by a factor that accounts for the solar azimuth angular dependence of H_{RTA} [14]. The fit is very good, as shown in Fig. 8(a), for band M1 in the high-gain stage and averaged over the detectors and both HAM sides. We also obtain a very good fit for using $H_{\mathrm{SDSM}}^{\mathrm{mea}}$ instead of H_{SDSM} in (25), as shown in Fig. 8(b). However, the F_2s from the two fits are not the same with the F_2 through H_{SDSM} increasing faster with time in the early mission, resulting in the F_2 larger by approximately 0.7% at later times. Consequently, by using H_{SDSM} and (25), the retrieved Earth spectral reflectance is approximately 0.7% higher at recent times, than using $H_{\mathrm{SDSM}}^{\mathrm{mea}}$ and (25).

VII. CONCLUSION

The SNPP VIIRS solar diffuser BRDF on-orbit change factor, the H-factor, is measured by the onboard solar diffuser stability monitor. Because the spectral response function of an SDSM detector does not behave exactly as a Dirac delta function in wavelength, the measured H-factor is not exactly the true H-factor at the detector center wavelength. In this paper, we have used two approaches to deconvolve the measured H-factor to obtain the true H-factor. The first approach is the popular direct method, relating the true H-factors to the measured ones through a set of linear equations that can be easily solved. The second approach is an innovative iterative method, relying on the properties of the dominance of the in-band contribution of the spectral response function's integral with respect to the wavelength and the narrow range of the in-band wavelengths so that over the range the H-factor does not vary excessively. We have shown that the deconvolved H-factors from the iterative approach are less affected by noises in the measured H-factors. Through an example in which the true H-factor follows a wavelength power law with an exponent of 4, we have shown that our iterative approach deconvolves the H-factors more accurately than the direct method for all the SDSM detectors, giving an accuracy equal to or better than 0.05% whereas the accuracy from the direct method is much worse, at approximately 0.59% for the SDSM detector 1. The iterative approach is also much more flexible in terms of interpolation and extrapolation of functional values. Deconvolving the H-factor with the iterative approach is quite fast. By using IDL code, the iterative approach needs approximately 10 s to deconvolve 2761 sets of H-factors on a Dell Precision 7820 Tower workstation, much faster than the direct method. We have used deconvolved H-factors in the SNPP VIIRS RSB calibration [14], [15], [23] for the NASA Collections 1 and 2 SNPP VIIRS Level-1B products. Finally, our iterative approach may also apply in areas such as x-ray scattering studies of materials [24].

APPENDIX A

We determine the change of $\mathrm{SR}_{\mathrm{SDSM}}(\lambda, t, d)\Phi_{\mathrm{SUN}}(\lambda, t)$ since the satellite launch, using the normalized SDSM detector Sun view digital count [14]. The SDSM detectors view the Sun through a screen (the SDSM screen) with through holes, as shown in Fig. 1. The SDSM screen relative effective transmittance is accurately determined by using both the yaw maneuver and regular SDSM on-orbit calibration data [25]. The change of $\mathrm{SR}_{\mathrm{SDSM}}(\lambda, t, d)\Phi_{\mathrm{SUN}}(\lambda, t)$ since the satellite launch is given by

$$\frac{dc_{\mathrm{SUN,norm}}(t,d)}{dc_{\mathrm{SUN,norm}}(t=0,d)} = \frac{\int_0^{\infty} d\lambda \times \mathrm{SR}_{\mathrm{SDSM}}(\lambda,t,d)\Phi_{\mathrm{SUN}}(\lambda,t)}{\int_0^{\infty} d\lambda \times \mathrm{SR}_{\mathrm{SDSM}}(\lambda,t=0,d)\Phi_{\mathrm{SUN}}(\lambda,t=0)}, \tag{A.1}$$

where $dc_{\mathrm{SUN,norm}}$ is the SDSM detector digital count when viewing the Sun through the SDSM screen, adjusted for the screen relative effective transmittance and the distance between the VIIRS and the Sun [14].

ACKNOWLEDGMENTS

We thank Amit Angal of the Science Systems and Applications, Inc., Lanham, MD USA (SSAI) for providing the lunar F-factors. We also thank Gal Sarid and Junqiang Sun of SSAI for review comments.

REFERENCES

[1] C. Schueler, J. Clement, P. Ardanuy, C. Welsch, F. DeLuccia, and H. Swenson, "NPOESS VIIRS sensor design overview", in *Proc. SPIE*, Vol. 4483, pp. 11-23, 2012; doi: 10.1117/12.453451.

[2] R. P. Murphy, P. E. Ardanuy, F. De Luccia, J. E. Clement, and C. Schueler, "The visible infrared imaging radiometer suite", in *Earth Science Satellite Remote Sensing*, J. Qu, W. Gao, M. Kafatos, R. Murphy, V. Salomonson, Ed., Vol. 1, pp. 199-223, Springer-Verlag: New York, USA, 2006.

[3] C. Cao, F. J. De Luccia, X. Xiong, R. Wolfe, and F. Weng, "Early On-Orbit Performance of the Visible Infrared Imaging Radiometer Suite Onboard the Suomi National Polar-Orbiting Partnership(S-NPP) Satellite", *IEEE Trans. Geosci. Remote Sens.*, Vol. 52, pp. 1142-1156, 2013; doi: 10.1109/TGRS.2013.2247768.

[4] X. Xiong, J. Sun, W. Barnes, W. Salononson, J. Esposito, H. Erives, and B. Guenther, "Multiyear On-Orbit Calibration and Performance of Terra MODIS Reflective Solar Bands", *IEEE Trans. Geosci. Remote Sens.*, Vol. 45, pp. 879-889, 2007; doi: 10.1109/TGRS.2006.890567.

[5] X. Xiong, J. Sun, X. Xie, W. Barnes, and V. Salomonson, "On-Orbit Calibration and Performance of Aqua MODIS Reflective Solar Bands", *IEEE Trans. Geosci. Remote Sens.*, Vol. 48, pp. 535-546, 2010; doi: 10.1109/TGRS.2009.2024307.

[6] Joint Polar Satellite System (JPSS) VIIRS Radiometric Calibration Algorithm Theoretical Basis Document (ATBD); NASA Goddard Space Flight Center: Greenbelt, MD, USA, 2013.

[7] R. E. Wolfe, G. Lin, M. Nishihama, K. Tewari, J. Tilton, and A. Isaacman, "Suomi NPP VIIRS prelaunch and on-orbit geometric calibration and characterization", *J. Geophy. Res.: Atmosphere*, Vol. 118, pp. 11508-11521, 2013; doi: 10.1002/jgrd.50873.

[8] G. Lin, R. Wolfe, J. Tilton, P. Zhang, J. Dellomo, and B. Tan, "JPPP-1/NOAA_20 VIIRS early on-orbit geometric performance", in *Proc. SPIE*, Vol. 10764, Art ID: 10764-1H, 2018; doi: 10.1117/12.2320767.

[9] N. Lei, Z. Wang, and X. Xiong, "On-orbit Radiometric Calibration of Suomi NPP VIIRS Reflective Solar Bands through Observations of a Sunlit Solar Diffuser Panel", *IEEE Trans. Geosci. Remote Sens.*, Vol. 53, pp. 5983-5990, 2015; doi: 10.1109/TGRS.2015.2430814.

[10] J. Fulbright, N. Lei, B. Efremova, and X. Xiong, "Suomi-NPP VIIRS Solar Diffuser Stability Monitor Performance", *IEEE Trans. Geosci. Remote Sens.*, Vol. 54, pp. 631-639, 2016; doi: 10.1109/TGRS.2015.2441558.

[11] R. Mammone, "Image Restoration Using Linear Programming," in *Image Recovery Theory and Application*, H. Stark, Ed. New York: Academic Press, Inc., 1987, pp. 127-156.

[12] P. Jansson, "Traditional Linear Deconvolution Methods," in *Deconvolution of Images and Spectra*, 2nd, ed., P. Jansson, New York: Dover Publications, Inc., 2012, pp. 76-106.

[13] W. Chen, and B. Gao, "A Multispectral Decomposition Technique for the Recovery of True SeaWiFS Top-of-Atmosphere Radiances", *IEEE Trans. Geosci. Remote Sens. Lett*, Vol. 10, pp. 288-292, 2013; doi: 10.1109/LGRS.2012.2203293.

[14] N. Lei, X. Xiong, Z. Wang, S. Li, and K. Twedt, "SNPP VIIRS RSB on-orbit radiometric calibration algorithms Version 2.0 and the performances, part 1: the algorithms," *J. Appl. Remote Sens.* Vol 14**,** Art-ID: 047501, 2020; doi: 10.1117/1.JRS.14.047501.

[15] N. Lei, X. Xiong, Z. Wang, S. Li, and K. Twedt, "SNPP VIIRS RSB on-orbit radiometric calibration algorithms Version 2.0 and the performances, part 2: the performances," *J. Appl. Remote Sens.* Vol 14**,** Art-ID: 047502, 2020; doi: 10.1117/1.JRS.14.047502.

[16] N. Lei, Z. Wang, J. Fulbright, and X. Xiong, "Effect of the SDSM detector relative spectral response in determining the degradation coefficient of the SNPP VIIRS Solar Diffuser reflectance", in *Proc. SPIE*, Vol. 8866, Art ID 8866-1I, 2013.

[17] N. Lei and X. Xiong, "Suomi NPP VIIRS Solar Diffuser BRDF Degradation Factor at Short Wave Infrared Band Wavelengths", *IEEE Trans. Geosci. Remote Sens.*, Vol. 54, pp. 6212-6216, 2016; doi: 10.1109/TGRS.2016.2583220.

[18] P. van Cittert, "About the influence of the gap width on the intensity distribution in spectral lines: II", *Z. Phys.* Vol. 69, pp. 298-308, 1931.

[19] X. Shao, T. Liu, X. Xiong, C. Cao, T. Choi, and A. Angal, "Surface Roughness-Induced Spectral Degradation of Multi-Spaceborne Solar Diffusers Due to Space Radiation Exposure", *IEEE Trans. Geosci. Remote Sens.*, Vol. 57, pp. 8658-8671, 2019; doi: 10.1109/TGRS.2019.2922070.

[20] N. Lei, K. Twedt, X. Xiong, and A. Angal, "Performance of NOAA-20 VIIRS Solar Diffuser and Solar Diffuser Stability Monitor", *IEEE Trans. Geosci. Remote Sens.*, in early access, doi: 10.1109/TGRS.2020.3032068.

[21] X. Xiong, J, Sun, J. Fulbright, Z. Wang, and J. Butler, "Lunar Calibration and Performance for S-NPP VIIRS Reflective Solar Bands," *IEEE Trans. Geosci. Remote Sens.*, **54** (2), pp. 1052-1061, 2016; doi: 10.1109/TGRS.2015.2473665.

[22] Z. Wang, X. Xiong, and Y. Li, "Improved VIIRS Band-to-band Registration Characterization based on Lunar Observation," *Remote Sens.*, **8**(1), pp. 27, 2016; doi: 10.3390/rs8010027.

[23] N. Lei, X. Xiong, Q. Mu, S. Li, and T. Chang, "Positional Dependence of SNPP VIIRS Solar Diffuser BRDF Change Factor", *IEEE Trans. Geosci. Remote Sens.*, Jan. 2021 (Early Access); doi: 10.1109/TGRS.2021.3050623.

[24] N. Lei, S. Safinya, and R. Bruinsma, "Discrete Harmonic Model for Stacked Membranes: Theory and Experiment", *J. Phys. B*, Vol. 5, 1995; doi: 10.1051/jp2:1995174.

[25] N. Lei, X. Chen, and X. Xiong, "Determination of the SNPP VIIRS SDSM Screen Relative Transmittance from Both Yaw Maneuver and Regular On-Orbit Data", *IEEE Trans. Geosci. Remote Sens.*, Vol 54, pp. 1390-1398, 2016; doi: 10.1109/TGRS.2015.2480039.